

Fusion of $^{35,37}\text{Cl} + ^{130}\text{Te}$ and subsequent fragmentation near the Coulomb barrier

Jagdeep Kaur,¹ Amandeep Kaur,² Gudveen Sawhney ,^{3,*} Manjeet Singh Gautam,⁴
Mahinder Pal Sharma,¹ BirBikram Singh,¹ and Manoj K. Sharma³

¹*Department of Physics, School of Basic and Applied Sciences, RIMT University, Mandi Gobindgarh 140406, Punjab, India*

²*Chitkara University Institute of Engineering and Technology, Chitkara University, Punjab 140401, India*

³*Department of Physics and Materials Science, Thapar Institute of Engineering and Technology, Patiala 147004, India*

⁴*Department of Physics, Government College Alewa (Jind) 126102, Haryana, India*



(Received 5 January 2024; accepted 13 February 2024; published 4 April 2024)

Extending from previous research where formation and decay analysis was carried out for even mass nuclei, this investigation includes the fusion-fragmentation analysis of odd mass isotopic compound systems, $^{165,167}\text{Tm}^*$, formed in reactions induced by $^{35,37}\text{Cl}$ projectiles carrying energy spanning the Coulomb barrier region ($E_{\text{c.m.}} = 90$ to 125 MeV), offering valuable insights into the reaction dynamics of these nuclear systems. To analyze the fusion dynamics of $^{35,37}\text{Cl} + ^{130}\text{Te}$ reactions, the energy-dependent Woods-Saxon potential (EDWSP) model is utilized and it introduces alterations in the potential barrier characteristics of the fusing nuclei. This results in the reduction of the effective fusion barrier, and accordingly influences the fusion outcomes. In contrast to the one-dimensional barrier penetration model (BPM), the EDWSP calculations yield enhanced fusion cross sections. This augmentation is especially evident in the energy-dependent behavior of cross sections for the selected fusion reactions, both in the near and sub-barrier energy domains. Furthermore, to address the decay of compound nuclei $^{165,167}\text{Tm}^*$, the evaporation residue (ER) cross sections are meticulously addressed for quadrupole (β_2) deformed fragments with orientations optimized for hot configurations, using the DCM model. The sub-barrier fusion enhancement in the excitation functions of lighter isotope $^{165}\text{Tm}^*$ are explored in terms of preformation and penetration profiles. Lastly, comparative studies of odd mass nuclear systems $^{165,167}\text{Tm}^*$ are carried out with even mass systems generated in Ca and Ni induced reactions.

DOI: [10.1103/PhysRevC.109.044607](https://doi.org/10.1103/PhysRevC.109.044607)

I. INTRODUCTION

Nuclear fusion relies on quantum tunneling, where colliding nuclei overcome interaction barriers through quantum wave behavior. The nonzero tunneling probability, a result of the wavelike nature of colliding partners, is crucial for fusion yields. This interplay, dependent on the radial characteristics of the interaction barrier at near- and sub-barrier energies, significantly impacts fusion cross sections and enhances our understanding of fusion reactions [1–6]. The phenomenon of complete fusion between colliding partners leads to the formation of a stable and enduring compound nucleus (CN) that eventually loses any trace of its initial formation process. This CN undergoes subsequent deexcitation through distinct channels, including the emission of light particles (LPs) or evaporation residue (ER), generation of intermediate mass fragments (IMFs), or the production of heavy mass fragments (HMFs) or fission fragments (ffs), which are described by various statistical evaporation [7–9] and fission models [10,11]. The specific decay pathway adopted by the CN is contingent upon several factors, including the energy of the incoming channel ($E_{\text{c.m.}}$), the angular momentum transferred to the CN, its mass and deformation, and the orientation of the decaying

fragments. Furthermore, the choice of CN decay is intricately linked to additional nuclear parameters and characteristics, such as level density. This multifaceted interplay of factors contributes to the rich variety of observed decay modes in the fusion process, providing valuable insights into the underlying nuclear dynamics.

The exploration of formation and decay processes is crucial, especially within the low-energy regime near the Coulomb barrier. Recent studies extensively investigated fusion-fragmentation (or fusion-evaporation) dynamics, focusing on even mass isotopic compound nuclei such as $^{98,104}\text{Cd}^*$ [12] and $^{122,128}\text{Ba}^*$ [13], produced in reactions induced by projectiles with magic shell closures such as ^{40}Ca and ^{64}Ni . Employing the energy-dependent Woods-Saxon potential (EDWSP) model [14–16] and the coupled-channels model for fusion analysis, and the dynamical cluster-decay model (DCM) [17–26] for decay patterns, these studies have yielded valuable insights. Building on this foundation, the present research extends this approach to investigate the fusion-fragmentation (or fusion-evaporation) dynamics of the odd mass isotopic compound nucleus $^{165,167}\text{Tm}^*$ formed in nuclear reactions involving an odd mass projectile combination ($^{35,37}\text{Cl} + ^{130}\text{Te}$) [27,28]. This extension enhances our understanding of fusion processes, particularly in systems with odd mass configurations, and contributes valuable insights in the energy range spanning the Coulomb barrier,

* gudveen.sahni@gmail.com

highlighting the role of the single unpaired nucleon. The fusion cross section (σ_F) refers here to the total decay cross section including contributions from the evaporation channel (σ_{ER}) and the fission channel (σ_{ff}), hence it is given as

$$\sigma_F = \sigma_{ER} + \sigma_{ff}. \quad (1)$$

For the chosen system, the fission contribution is negligible so the total fusion cross sections $\sigma_F \simeq \sigma_{ER}$. In this case, σ_F is estimated by the energy-dependent Woods-Saxon potential (EDWSP) model and the ER channel cross sections are estimated by the collective clusterization technique of the dynamical cluster-decay model (DCM).

In fusion studies, experimental fusion cross sections [4–6] consistently surpass predictions from the one-dimensional barrier penetration model (BPM) by orders of magnitude. The BPM, neglecting internal structure degrees of freedom, particularly struggles in the sub-barrier energy region. Internal degrees of freedom, such as vibrational states, static deformations, nucleon transfer, and entrance channel asymmetry, significantly contribute to sub-barrier fusion enhancement [29–31]. Coupled-channels models [32–36] effectively replicate experimental data, but complexities arise with numerous intrinsic channels. Alternative theoretical methods, including Hartree-Fock theory [37–39], the symmetric-asymmetric Gaussian barrier distribution (SAGBD) model [40–44], mean-field theories [45], energy density functional (EDF) theory [46–50], and the energy-dependent Woods-Saxon potential (EDWSP) model [14–16], provide diverse approaches to capture these effects. Recent studies extensively investigate the role of inelastic surface excitations and static deformation in various projectile-target combinations, consistently favoring sub-barrier fusion enhancement. While positive Q -value neutron transfer channels in certain reactions contribute to additional sub-barrier enhancement [29–31], their role remains puzzling and warrants further investigation. Experimental fusion cross sections of $^{35,37}\text{Cl} + ^{130}\text{Te}$ reactions [27,28] confirm sub-barrier enhancements attributed to low-lying vibrational states and neutron transfer channels. The EDWSP model, considering the energy-dependent Woods-Saxon potential, comprehensively addresses barrier characteristics, offering insights into fusion reactions, including the relative sub-barrier enhancement observed in $^{35}\text{Cl} + ^{130}\text{Te}$ over $^{37}\text{Cl} + ^{130}\text{Te}$ reactions.

Further, this study explores the investigation of the decay of compound nuclei $^{165,167}\text{Tm}^*$, formed through fusion reactions involving $^{35}\text{Cl} + ^{130}\text{Te}$ and $^{37}\text{Cl} + ^{130}\text{Te}$ [27,28], spanning the energy region of $E_{c.m.} = 90\text{--}125$ MeV. The dynamical cluster-decay model (DCM) [17–26] is employed to comprehensively analyze this decay process. The experimental results reveal that the excitation functions for the decay of these compound systems exhibit contribution from evaporation residue channel. The DCM proves to be a successful model in addressing these cross sections. In this research, calculations specifically focus on quadrupole-deformed (β_2 -deformed) fragments, optimizing their orientations for hot configurations. To ensure accuracy, the neck-length parameter is meticulously fine tuned to align with the experimental cross sections within the theoretical framework, showcasing excellent agreement with the empirical data. The scope of

the analysis extends across both below- and above-barrier energy regions. The intricacies of barrier profiles, fragmentation structures, preformation, and barrier penetration plots are systematically explored. Furthermore, the impact of the energy of the incoming channel and angular momentum on these profiles is investigated, extracting valuable insights. In the final stages of the investigation, a comparative study of the decay profile of odd mass nuclear systems is conducted, drawing parallels and distinctions with even mass nuclear systems. This comparative approach enhances the understanding of the role played by unpaired nucleons in influencing the decay dynamics. Through this comprehensive exploration, the study aims to contribute valuable insights to the field of nuclear reactions at low energies, shedding light on the complex mechanisms governing the decay of compound nuclei

The paper is structured as follows: In Sec. II, we present the methodology employed for conducting the calculations in this study, in two distinct subsections. Section II A outlines the theoretical framework used to investigate the fusion process, specifically the energy-dependent Woods-Saxon potential (EDWSP) model. Then, Sec. II B elaborates on the methodology employed for conducting the decay analysis, focusing on the dynamical cluster-decay model (DCM).

Section III is dedicated to the discussion of our calculations and the corresponding results. Finally, in Sec. IV, we provide a succinct summary of the key findings and conclusions drawn from the present work.

II. METHODOLOGY

The methodology is divided into two parts. In part A, the fusion criteria is explained briefly whereas the subsequent decay analysis is covered in part B.

A. Formation process

The partial wave fusion cross sections are described by the equation

$$\sigma_F = \frac{\pi}{k^2} \sum_{\ell} (2\ell + 1) T_{\ell}^F. \quad (2)$$

Here, the tunneling probability (T_{ℓ}^F) can be determined either through numerical solutions of the Schrödinger wave equation or via the parabolic approximation of the effective interaction between colliding nuclei [51], represented as

$$T_{\ell}^{HW} = \frac{1}{\left[1 + \exp\left(\frac{2\pi}{\hbar\omega_{\ell}}(V_{\ell} - E_{c.m.})\right)\right]}. \quad (3)$$

In this context, $E_{c.m.}$, V_{ℓ} , and $\hbar\omega_{\ell}$ correspond to the incident energy in the center-of-mass frame, barrier height, and barrier curvature for the ℓ th partial wave, respectively. Wong [52] further refined this parabolic approximation by considering contributions from an infinite number of partial waves to the fusion process and by incorporating approximations for barrier position, barrier curvature, and barrier height, yielding

the final expression for fusion cross-section evaluation:

$$\sigma_F = \frac{\hbar\omega}{2E_{c.m.}} R_B^2 \ln \left[1 + \exp \left(\frac{2\pi}{\hbar\omega} (E_{c.m.} - V_{B0}) \right) \right]. \quad (4)$$

In this equation, R_B , $\hbar\omega$, and V_{B0} represent the barrier position, barrier curvature, and barrier height for the Coulomb barrier.

The nucleus-nucleus potential forms the basis of theoretical calculations, with the energy-dependent Woods-Saxon potential (EDWSP) [14–16] used in conjunction with the Wong formula [52] for fusion process calculations. The static form of the Woods-Saxon potential is defined as

$$V_N(r) = \frac{-V_0}{\left[1 + \exp \left(\frac{R-R_0}{a} \right) \right]}. \quad (5)$$

In the EDWSP approach, the depth of the real part of the Woods-Saxon potential is defined by

$$V_0 = [(A_P^{2/3} + A_T^{2/3}) - (A_P + A_T)^{2/3}] \times \left[2.38 + 6.8(1 + I_P + I_T) \frac{A_P^{1/3} A_T^{1/3}}{(A_P^{1/3} + A_T^{1/3})} \right] \text{MeV}, \quad (6)$$

$$a(E_{c.m.}) = 0.85 \left[1 + \frac{r_0}{\left\{ 13.75(A_P^{-1/3} + A_T^{-1/3}) \left[1 + \exp \left(\frac{E_{c.m.} - 0.96}{\frac{V_{B0} - 0.96}{0.03}} \right) \right] \right\}} \right] \text{fm}. \quad (8)$$

In the EDWSP calculations, the potential parameters such as depth (V_0), range (r_0), and diffuseness (a) of the Woods-Saxon potential are interrelated. Adjusting one parameter entails corresponding changes in the other two. The depth (V_0) significantly depends on surface energy and isospin. Range and diffuseness parameters are linked by Eq. (7). The range parameter (r_0) is associated with the radii of fusing nuclei through $R_0 = r_0(A_P^{1/3} + A_T^{1/3})$, which in turn depends on nuclear shape. The value of the range parameter is sensitive to the nature of interacting nuclei and dominant nuclear structure degrees of freedom, leading to variations for different projectile-target combinations. The range parameters for the studied reactions lie within the range of 0.90 to 1.35 fm, consistent with values used in different approaches [1–6,29–31].

The EDWSP fusion barrier is defined by the equation

$$V_{B0}^{\text{EDWSP}} = V_N(r = R_B) + V_C(r = R_B) \quad (9)$$

where

$$V_{B0}^{\text{EDWSP}} = \frac{-V_0}{\left[1 + \exp \left(\frac{R_B - R_0}{a(E_{c.m.})} \right) \right]} + \frac{Z_P Z_T e^2}{R_B}. \quad (10)$$

In the EDWSP model, the calculations utilize Eq. (5) with V_{B0} replaced by the EDWSP fusion barrier height (V_{B0}^{EDWSP}) as defined in the above equations.

where $I_P = \frac{N_P - Z_P}{A_P}$ and $I_T = \frac{N_T - Z_T}{A_T}$ are the isospin asymmetries of the projectile and target nuclei, respectively. The Coulomb potential V_C for spherical nuclei is given by

$$V_C = \frac{Z_P Z_T e^2}{r}. \quad (7)$$

In the realm of heavy-ion fusion dynamics, an array of static and dynamic effects come into play, including variations in the N/Z ratio, surface energy, surface diffuseness of colliding pairs, density profile variations in the neck region, and the dissipation of kinetic energy of relative motion into internal structure degrees of freedom. The isotopic dependence of sub-barrier fusion enhancement is directly manifested when a common projectile is incident on a series of target isotopes or vice versa. These physical factors necessitate modifications in the parameters of the static Woods-Saxon potential, particularly requiring larger diffuseness to account for sub-barrier fusion data [53,54]. The energy dependence in the nucleus-nucleus potential is attributed to effective nucleon-nucleon interactions and nonlocal quantum effects [55,56], involving nucleon exchange between colliding nuclei and leading to velocity-dependent nuclear potentials. To address these complexities, the energy dependence in the Woods-Saxon potential is introduced via its diffuseness parameter, defined as

B. Dynamical cluster-decay model (DCM)

The dynamical cluster-decay model (DCM) [17–26] represents an extension of the preformed cluster model (PCM) [57–59], which is specifically designed for describing radioactive processes and spontaneous emissions. Grounded in the established quantum mechanical fragmentation theory (QMFT) [60–62], the DCM employs collective coordinates such as mass asymmetry $\eta_A = \frac{A_1 - A_2}{A_1 + A_2}$, relative separation R , multipole deformations β_i ($\lambda = 2, 3, 4$), and orientations θ_i of decaying fragments as fundamental components.

The preformation probability P_0 encapsulates the anticipation that the decaying fragments are preformed within the compound nucleus, serving as a conduit for the structural characteristics of the exit channel. The preformation probability is obtained by solving the stationary Schrödinger equation in mass coordinates (η), specifically at $R = R_a$, given by

$$\left[-\frac{\hbar^2}{2\sqrt{B_{\eta\eta}}} \frac{\partial}{\partial \eta} \frac{1}{\sqrt{B_{\eta\eta}}} \frac{\partial}{\partial \eta} + V_R(\eta, T) \right] \psi^\nu(\eta) = E_\eta^\nu \psi^\nu(\eta), \quad (11)$$

The resulting solution provides the preformation probability (P_0), defined as

$$P_0 = |\psi(\eta(A_i))|^2 \sqrt{B_{\eta\eta}} \frac{2}{A_{CN}} \quad (12)$$

where both ground state ($\nu = 0$) and excited states ($\nu = 1, 2, 3, \dots$) are considered, and $|\psi(\eta(A_i))\rangle$ is a Boltzmann-like function. The mass parameters $B_{\eta\eta}$ employed here correspond to the hydrodynamical masses of Kröger and Scheid [63], constituting the kinetic energy aspect of the Schrödinger wave equation. The potential term used for solving the Schrödinger equation is the temperature-dependent fragmentation potential, defined as

$$V_R(\eta, T) = \sum_{i=1}^2 [B_i(A_i, Z_i, T)] + \sum_{i=1}^2 [\delta U_i] \exp(-T^2/T_0^2) \\ + V_C(R, Z_i, \beta_{\lambda i}, \theta_i, T) + V_P(R, A_i, \beta_{\lambda i}, \theta_i, T) \\ + V_\ell(R, A_i, \beta_{\lambda i}, \theta_i, T). \quad (13)$$

In this equation, B_i ($i = 1, 2$) refers to the LDM binding energies derived from the semiempirical mass formula by Seeger [64], made temperature-dependent following the approach of Davidson *et al.* [65]. The empirical shell corrections (δU_i) are obtained from Myers and Swiatecki [66], accounting for the microscopic part of binding energies. Additionally, the potential includes temperature-dependent Coulomb, nuclear proximity, and centrifugal potential terms for deformed oriented nuclei.

The barrier tunneling probability, also known as barrier penetration probability, is evaluated using the quantum Wentzel-Kramers-Brillouin (WKB) approach:

$$P = \exp \left[-\frac{2}{\hbar} \int_{R_a}^{R_b} 2\mu [V(R) - Q_{\text{eff}}]^{1/2} dR \right], \quad (14)$$

where $V(R_a, T) = V(R_b, T) = \text{TKE}(T) = Q_{\text{eff}}$ for the two turning points. Here, Q_{eff} represents the effective Q value of the decay process.

The decay cross sections are formulated based on the preformation probability (P_0) and penetration probability (P), expressed as

$$\sigma = \sum_{\ell=0}^{\ell_{\text{max}}} \sigma_\ell = \frac{\pi}{k^2} \sum_{\ell=0}^{\ell_{\text{max}}} (2\ell + 1) P_0 P, \quad \text{where } k = \sqrt{\frac{2\mu E_{\text{c.m.}}}{\hbar^2}}. \quad (15)$$

The Schrödinger wave equation, decoupled as described earlier, is solved at the first turning point R_a , which is defined as

$$R_a = R_1(\alpha_1, T) + R_2(\alpha_2, T) + \Delta R(T) = R_i(\alpha, T) + \Delta R(T) \quad (16)$$

The parameter ΔR within the expression for R_a contributes to defining the effective ‘‘barrier lowering’’ parameter $\Delta V_B(\ell)$ at each ℓ , reflecting the difference between the actual barrier $V_B(\ell)$ and the calculated barrier $V(R_a, \ell)$ as $\Delta V_B = V(R_a, \ell) - V_B(\ell)$.

III. CALCULATIONS AND DISCUSSION OF RESULTS

This section is bifurcated into two segments. Part A delves into the exploration of the fusion mechanism of $^{35,37}\text{Cl} + ^{130}\text{Te}$ reactions, employing the EDWSP model [14–16]. Subsequently, in part B, an in-depth analysis of the

resulting decay patterns is conducted, utilizing the dynamical cluster-decay model (DCM) [17–26].

A. Fusion study of $^{35}\text{Cl} + ^{130}\text{Te}$ and $^{37}\text{Cl} + ^{130}\text{Te}$ reactions

In EDWSP analysis, for the $^{35}\text{Cl} + ^{130}\text{Te}$ reaction at the lowest incident energy ($E_{\text{c.m.}} = 90$ MeV) and largest diffuseness parameter ($a = 0.982$ fm), the calculated lowest energy-dependent fusion barrier (LEDFB) is 98.767 MeV. Similarly, for the $^{37}\text{Cl} + ^{130}\text{Te}$ reaction under the same conditions ($E_{\text{c.m.}} = 90$ MeV, $a = 0.981$ fm), the LEDFB is 99.163 MeV. These LEDFB values are notably smaller than the respective Coulomb barriers, which are 105.210 MeV for $^{35}\text{Cl} + ^{130}\text{Te}$ and 104.240 MeV for $^{37}\text{Cl} + ^{130}\text{Te}$. The difference between the EDWSP-calculated LEDFB and the Coulomb barrier is -6.443 MeV for $^{35}\text{Cl} + ^{130}\text{Te}$ and -5.077 MeV for $^{37}\text{Cl} + ^{130}\text{Te}$. This difference is more significant for the lighter projectile (^{35}Cl) compared to the heavier one, indicating a relatively larger sub-barrier fusion enhancement for $^{35}\text{Cl} + ^{130}\text{Te}$. As the incident energy increases, the diffuseness parameter decreases, reaching its lowest value (0.850 fm). This reduction in diffuseness leads to an increase in the energy dependent fusion barrier. The EDWSP model’s modulation of the diffuseness parameter at different energies is depicted in Fig. 1 for $^{35,37}\text{Cl} + ^{130}\text{Te}$ reactions, highlighting the relevance of dominant intrinsic channels during fusion at below barrier energies. Beyond the Coulomb barrier ($E_{\text{c.m.}} = 125$ MeV, $a = 0.850$ fm), the highest energy-dependent fusion barrier (HEDFB) produced in the EDWSP calculations remains considerably smaller than the corresponding Coulomb barrier (HEDFB = 102.264 MeV for $^{35}\text{Cl} + ^{130}\text{Te}$ and HEDFB = 102.180 MeV for $^{37}\text{Cl} + ^{130}\text{Te}$). This significant reduction in the interaction fusion barrier underscores the larger sub-barrier fusion enhancement predicted by the EDWSP calculations.

The fusion mechanisms of $^{35,37}\text{Cl} + ^{130}\text{Te}$ reactions are investigated using the EDWSP model. This model accounts for the effects of dominant channel couplings arising from the intrinsic properties of interacting nuclei, which are inherently incorporated due to the energy-dependent nature of the Woods-Saxon potential. Figure 1 illustrates the interaction barriers between the participating nuclei at various incident energies, revealing distinct barrier profiles. For the $^{35}\text{Cl} + ^{130}\text{Te}$ reaction, the conventional Woods-Saxon potential yields a single Coulomb barrier with parameters $V_{B0} = 105.210$ MeV, $R_B = 11.240$ fm, and $\hbar\omega = 4.400$ MeV. Similarly, for $^{37}\text{Cl} + ^{130}\text{Te}$, the parameters are $V_{B0} = 104.240$ MeV, $R_B = 11.650$ fm, and $\hbar\omega = 3.560$ MeV. These values are listed in Table I. The range, depth and diffuseness of the Woods-Saxon potential used in the EDWSP model calculations for the chosen reactions are shown in Table II. In contrast to the conventional potential, the energy-dependent Woods-Saxon potential assumes attractive characteristics, thus modifying the fusion barrier profiles for $^{35,37}\text{Cl} + ^{130}\text{Te}$ reactions around the Coulomb barrier. The EDWSP introduces a range of energy-dependent fusion barriers with varied heights and strengths (see Fig. 1). Notably, these energy-dependent fusion barriers are consistently lower than the Coulomb barrier, enhancing the EDWSP model’s ability to

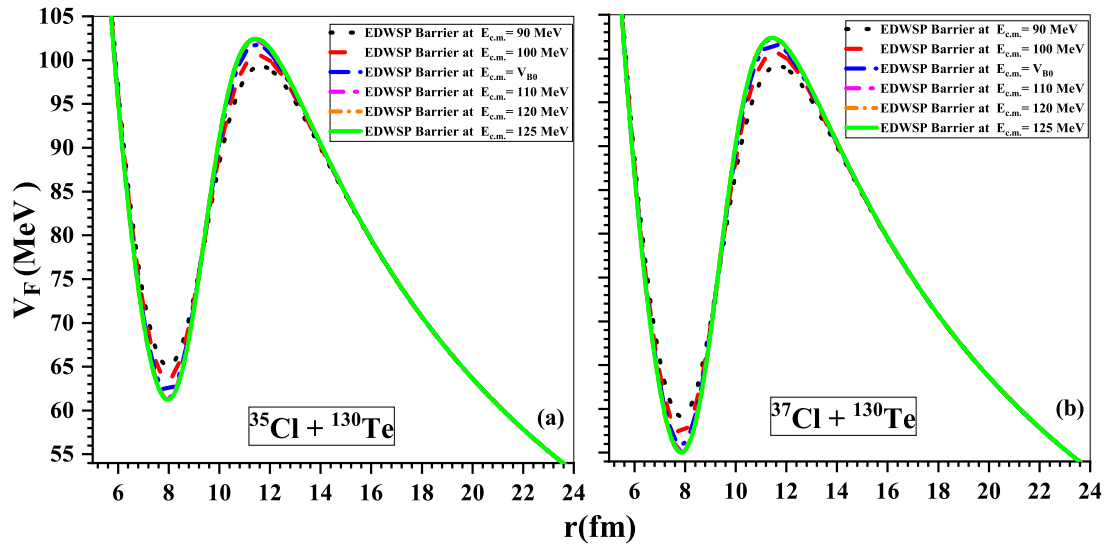


FIG. 1. Radial dependence of the fusion barrier for (a) $^{35}\text{Cl} + ^{130}\text{Te}$ and (b) $^{37}\text{Cl} + ^{130}\text{Te}$ reactions at different bombarding energy ($E_{c.m.}$) obtained by using the EDWSP model.

predict larger fusion cross sections compared to the one-dimensional barrier penetration model (BPM). The shape of the EDWSP fusion barrier heavily relies on the selection of range parameter (r_0) and diffuseness parameter. These parameters are sensitive to the intrinsic channels active in the tunneling process, influenced by the geometry and density profiles of the colliding nuclei. Variations in the diffuseness parameter directly impact the density distribution of nucleons during fusion, ultimately affecting the nucleus-nucleus potential strength in the domain of Coulomb barrier.

The EDWSP's adaptable diffuseness parameter modifies the interaction barrier between participants, leading to barrier-lowering effects. This effectively reduces the fusion barrier compared to the original Coulomb barrier, allowing the EDWSP to predict significantly increased fusion cross sections relative to the one-dimensional BPM. Thus, appropriate choice of range parameter (r_0) facilitates the necessary barrier modulation, enabling the EDWSP model to aptly capture the fusion mechanisms of $^{35,37}\text{Cl} + ^{130}\text{Te}$ reactions. The relevant results are presented in Figs. 2 and 3. Analogous barrier-lowering effects due to coupling between relative motion and inherent degrees of freedom were emphasized in Refs. [27,28]. The EDWSP predictions align well with experimental data such as coupled-channels outcomes predicted by the authors. This indicates that EDWSP results inherently encompass the impact of relevant channel couplings along the fusion path. Theoretical cross sections calculated using

the static Woods-Saxon potential and the energy-dependent Woods-Saxon potential (EDWSP) within the Wong formula are compared with the experimental data of $^{35,37}\text{Cl} + ^{130}\text{Te}$ reactions [27,28], as shown in Fig. 2. Deviations between theoretical cross sections using the standard Woods-Saxon potential and experimental data are prominent in the sub-barrier region, indicating missing intrinsic channels during tunneling. Predictions based on the simple Wong formula are notably smaller at energies lying below the Coulomb barrier. High Coulomb barrier height restricts fusion at lower energies, which is evident in theoretical predictions and becomes more pronounced at lowest energies (Fig. 2). This is a clear indication of contribution from low-lying inelastic excitations, deformations, and positive Q -value neutron transfer channels. Without considering aforementioned intrinsic channels, one cannot reproduce experimentally observed behaviors of fusion cross sections of $^{35,37}\text{Cl} + ^{130}\text{Te}$ reactions especially in near- and below-barrier regions. In Ref. [28], authors analyzed $^{37}\text{Cl} + ^{130}\text{Te}$ fusion using coupled-channels calculations, incorporating odd- A spin states of the projectile and vibrational states (2^+ , 3^-) of the target. For $^{35}\text{Cl} + ^{130}\text{Te}$ reaction [27], authors highlighted that, in addition to odd- A spin states of the projectile and low lying (2^+ , 3^-) vibrational states of target, the couplings to positive Q -value neutron transfer channels improve agreement with the fusion data. Among six neutron transfer channels, the one with +4.38 MeV Q value dominates

TABLE I. The parameters employed in the EDWSP model calculations for the analyzed reactions include the Coulomb barrier (V_{B0}), barrier position (R_B), and barrier curvature ($\hbar\omega$).

System	V_{B0} (MeV)	R_B (fm)	$\hbar\omega$ (MeV)
$^{35}\text{Cl} + ^{130}\text{Te}$	105.210	11.240	4.400
$^{37}\text{Cl} + ^{130}\text{Te}$	104.240	11.650	3.560

TABLE II. Range, depth and diffuseness of the Woods-Saxon potential used in the EDWSP model calculations for the chosen reactions.

System	r_0 (fm)	V_0 (MeV)	$\frac{\rho^{\text{Present}}}{\text{Energy Range}} \left(\frac{\text{fm}}{\text{MeV}} \right)$
$^{35}\text{Cl} + ^{130}\text{Te}$	1.115	119.209	$\frac{(0.982) \text{ to } (0.850)}{(90) \text{ to } (125)}$
$^{37}\text{Cl} + ^{130}\text{Te}$	1.100	128.098	$\frac{(0.981) \text{ to } (0.850)}{(90) \text{ to } (125)}$

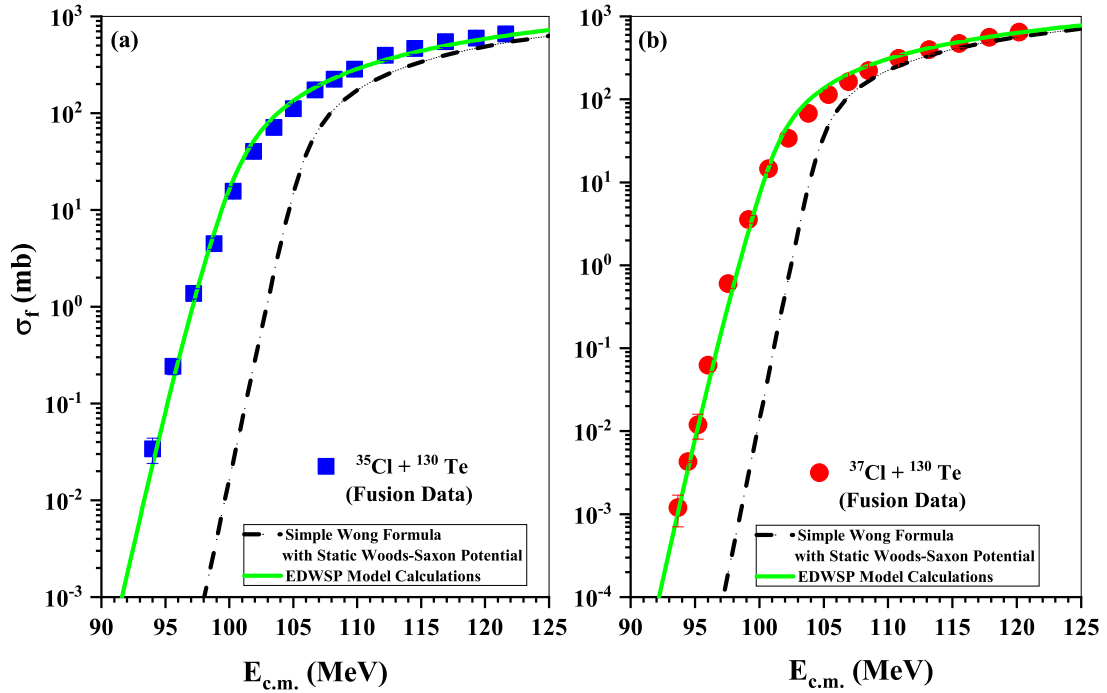


FIG. 2. The fusion cross sections as a function of $E_{c.m.}$ obtained for (a) $^{35}\text{Cl} + ^{130}\text{Te}$ and (b) $^{37}\text{Cl} + ^{130}\text{Te}$ reactions by using the EDWSP model and the experimental data taken from Refs. [27,28].

for $^{35}\text{Cl} + ^{130}\text{Te}$, while all are suppressed in $^{37}\text{Cl} + ^{130}\text{Te}$, explaining larger sub-barrier fusion in the former.

Further, the authors of Ref. [28] emphasized that the astrophysical S factor of $^{37}\text{Cl} + ^{130}\text{Te}$ reaction has not shown

maxima in low energy regions but exhibits continuous increase for the entire sub-barrier energy region. In order to solidify the above conclusion, the logarithmic derivative of the fusion cross-section data was also explored and was found

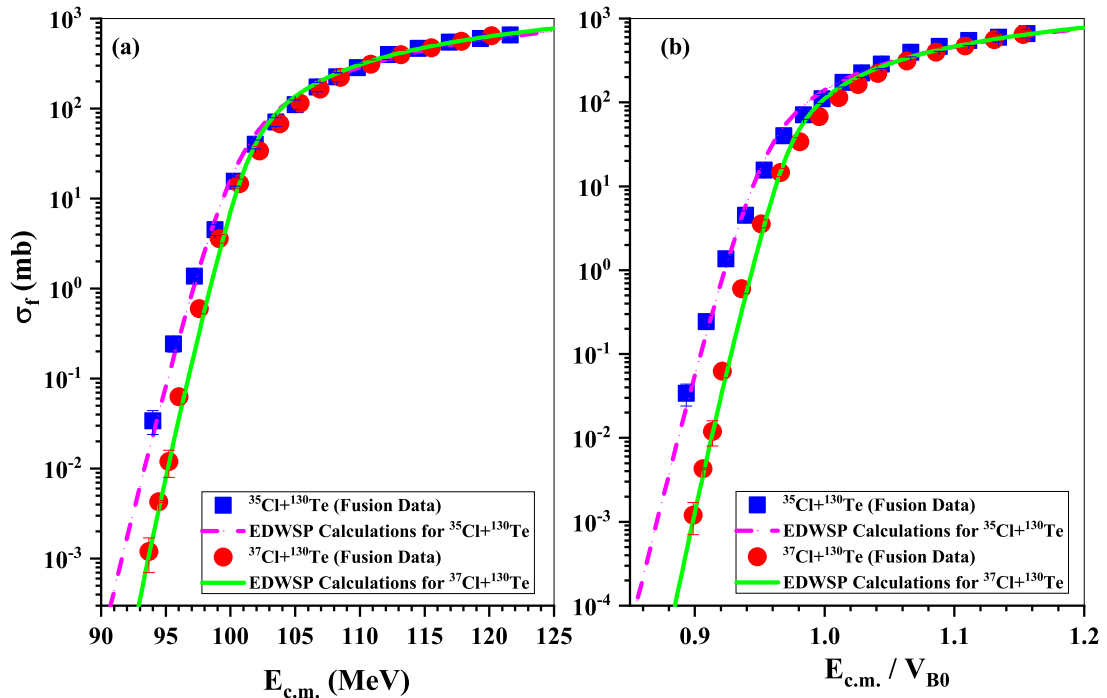


FIG. 3. Comparison of fusion cross sections as a function of $E_{c.m.}$ obtained for (a) $^{35,37}\text{Cl} + ^{130}\text{Te}$ reactions in normal scale and (b) $^{35,37}\text{Cl} + ^{130}\text{Te}$ reactions in reduced scale by using the EDWSP model and the experimental data taken from Refs. [27,28].

to follow an increasing trend with decrease in incident energy to the deep sub-barrier domain. The energy dependent representation of the astrophysical S factor and logarithmic derivative in the deep sub-barrier domain has shown the absence of fusion hindrance in the $^{37}\text{Cl} + ^{130}\text{Te}$ fusion reaction. The absence of fusion hindrance in the above system can be correlated with the existence of multiple fusion barriers appearing due to static and dynamic deformations, that leads to different turning points depending upon mutual orientations and excitations of the participant nuclei. In a similar sense, the absence of fusion hindrance in $^{35}\text{Cl} + ^{130}\text{Te}$ (unlike coupled-channels predictions), relates to two neutron transfer channels mitigating Pauli repulsion, enabling nuclear matter exchange and reducing the effective fusion barrier in the deep sub-barrier region. Simenel *et al.* [67] suggested that the Pauli repulsion effect during nucleon-nucleon interaction reduces the tunneling probability at deep sub-barrier energies along the fusion path. As a result, the fusion hindrance appears in the deep sub-barrier domain due to the steep fall-off of fusion cross sections, with reference to the standard coupled-channels predictions. The presence of a positive Q -value neutron transfer channel favors the fusion process by forming a neck between participants in the deep sub-barrier energy region and mitigates the Pauli repulsion effect. Similar conclusions regarding a positive Q -value neutron transfer channel are also inferred from the previous analysis [13].

In Fig. 3, a comparison between the fusion cross sections of $^{35,37}\text{Cl} + ^{130}\text{Te}$ reactions is depicted, both in regular energy scale and the reduced energy scale. The experimental data for $^{35,37}\text{Cl} + ^{130}\text{Te}$ reactions are augmented with theoretical estimations based on the EDWSP model, shown alongside the experimental data. The analysis indicates that the fusion cross sections of the $^{35}\text{Cl} + ^{130}\text{Te}$ reaction exhibit enhancement relative to $^{37}\text{Cl} + ^{130}\text{Te}$ reaction, particularly in the sub-barrier energy region. Notably, the presence of a positive Q -value neutron transfer channel prevents the sharp decrease in the fusion excitation function of the $^{35}\text{Cl} + ^{130}\text{Te}$ reaction at deep sub-barrier energies, as highlighted in Ref. [27]. The low-lying odd- A spin states of the projectiles are almost similar in strength, having the same excitation energies, and the target is common to both projectiles; both fusion reactions are expected to follow a similar trend. However, the difference in the sub-barrier fusion enhancement of $^{35,37}\text{Cl} + ^{130}\text{Te}$ reactions appeared typically due to the presence of the positive Q -value neutron transfer channel. In case of the $^{35}\text{Cl} + ^{130}\text{Te}$ reaction, six neutron transfer channels with positive Q value are allowed, and the pair neutron transfer channel having a positive Q value of +4.38 MeV is the dominant one. For the $^{37}\text{Cl} + ^{130}\text{Te}$ reaction, the neutron transfer channels with positive Q value are forbidden, thereby suppressing the effects of the neutron transfer channel. Henning *et al.* [68] emphasized that the conclusions due to positive Q -value neutron transfer channels become more unambiguous if one deals with optimum Q value instead of ground state Q value. In some cases, it has been observed that the ground state Q value is positive for neutron transfer channels but the corresponding optimum Q value is negative, and in such a case no additional sub-barrier fusion enhancement was found due to couplings of the positive Q -value neutron transfer channel. In this sense,

the neutron transfer channels with positive ground state Q value (or negative optimum Q value) for the neutron transfer channel turned out to show negligible or weak influence on the fusion process. However, the projectile-target combinations for which both ground state Q value and corresponding optimum Q value for neutron transfer channel are positive displayed strong additional sub-barrier fusion enhancement. This may be the possible reason why some fusing systems, besides having positive ground state Q value, do not demonstrate strong sub-barrier fusion enhancement due to couplings of positive Q -value neutron transfer channels. Sargsyan *et al.* [69,70], based on a quantum diffusion approach, pointed out that neutron transfer channels have weak impact on the fusion process if the deformation strength of fusing partners does not change or decreases after neutron transfer. However, if the deformation strength of fusing partners increases after neutron transfer then such projectile-target combinations display strong additional sub-barrier fusion enhancement due to couplings of neutron transfer channels. Hence, sub-barrier fusion enhancement due to inclusion of positive Q -value neutron transfer channels is quite sensitive to the change of deformation strength of the fusing partners after neutron transfer. In the chosen reactions, the projectile ^{37}Cl nucleus has fully occupied neutron shell ($1d_{3/2}$ and neutron number $N = 20$) while the ^{35}Cl nucleus has half occupied neutron shell ($1d_{3/2}$ and neutron number $N = 18$) and the ^{35}Cl nucleus facilitates the absorption of six neutrons with positive Q value. Among these, the two-neutron transfer channel with positive Q value of +4.38 MeV is the dominant one, and transferring a pair of neutrons from target (^{130}Te) to projectile (^{35}Cl) effectively reduces the fusion barrier between participants resulting in the enhanced fusion cross sections. Therefore, the present work suggests that the observed sub-barrier fusion enhancement of $^{35}\text{Cl} + ^{130}\text{Te}$ reaction relative to $^{37}\text{Cl} + ^{130}\text{Te}$ reaction appeared due to the populations of the positive Q -value neutron transfer channels in the $^{35}\text{Cl} + ^{130}\text{Te}$ reaction, signifying the importance of the neutron transfer channel in the fusion dynamics. The EDWSP model provides a suitable description of the energy-dependent behavior of the fusion cross sections for both reactions across the entire range of incident energies.

In Fig. 4, the variation of diffuseness parameter as a function of incident energy is shown for $^{35,37}\text{Cl} + ^{130}\text{Te}$ reactions. From this figure, it is clear that with the increase in incident energy the diffuseness parameter decreases and finally saturates to its lowest value (0.850 fm). For instance for $^{35}\text{Cl} + ^{130}\text{Te}$ ($^{37}\text{Cl} + ^{130}\text{Te}$) reaction, the diffuseness decreases from 0.982 (0.981) fm to 0.850 (0.850) fm as incident energy changes from 90 to 125 MeV. The diffuseness parameter defines the slope of the Woods-Saxon potential in the surface regions, and its choice directly or indirectly affects curvature and thickness of the effective fusion barrier between the participant nuclei. The energy-dependent nature of the Woods-Saxon potential brings different dynamical factors with various incident energy regimes. As a result, the energy-dependent nuclear potential generates quite analogous barrier lowering, as inferred from the inclusions of the inelastic surface excitations, static deformation, nucleon transfer channels, and other dynamical effects during quantum mechanical tunneling process. Hence, the variations of diffuseness with

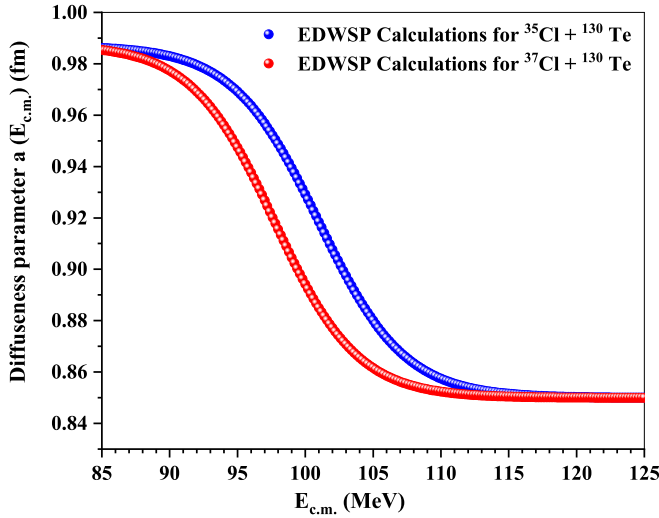


FIG. 4. Diffuseness parameter $a(E_{c.m.})$ calculated by EDWSP calculations plotted in terms of $E_{c.m.}$ for $^{35}\text{Cl} + ^{130}\text{Te}$ and $^{37}\text{Cl} + ^{130}\text{Te}$ reactions.

incident energy reflect strong influence of density distribution evolutions inside the composite system along the fusion path. Therefore, Fig. 4 clearly demonstrates the relevance of the energy dependence in the Woods-Saxon potential, and consequences of such energy dependence are barrier modifications and barrier lowering effects during quantum mechanical tunneling through the fusion barrier. The energy dependent nature of the Woods-Saxon potential, as appears in the EDWSP model, seems to be a true representation of the nuclear potential. This signifies that the impact of intrinsic degrees of freedom associated with the fusing pairs during the fusion process can be included in the theoretical estimations either by considering intrinsic channels directly in the coupled-channels formalism or by considering an energy-dependent interaction potential as in the EDWSP model. Both approaches modify quantum mechanical tunneling behavior through the interaction barrier in such a way that the original barrier gets reduced, resulting in the enhanced fusion cross sections relative to the output of the one-dimensional BPM.

In order to solidify the above conclusion, in Fig. 5 the radial profiles of the static Woods-Saxon potential and EDWSP fusion barriers are compared for a specific incident energy ($E_{c.m.} = 90$ and 125 MeV) for $^{35,37}\text{Cl} + ^{130}\text{Te}$ reactions. The EDWSP fusion barriers for the $^{35}\text{Cl} + ^{130}\text{Te}$ reaction (represented by the dash-dot blue color line at $E_{c.m.} = 90$ MeV and the dash-dot-dot magenta color line at $E_{c.m.} = 125$ MeV) appear notably shallower than the fusion barriers obtained from the static Woods-Saxon potential (dot-dot black color line) particularly at lower incident energies. Similarly, the EDWSP fusion barriers for the $^{37}\text{Cl} + ^{130}\text{Te}$ reaction (represented by the dash-dot cyan color line at $E_{c.m.} = 90$ MeV and the solid green color line at $E_{c.m.} = 125$ MeV) appear notably shallower than the fusion barrier obtained from the static Woods-Saxon potential (dash-dash red color line) especially at lower incident energies. This shallower nature of the EDWSP fusion barriers in the deep sub-barrier energy region can be attributed to the Pauli repulsion effect

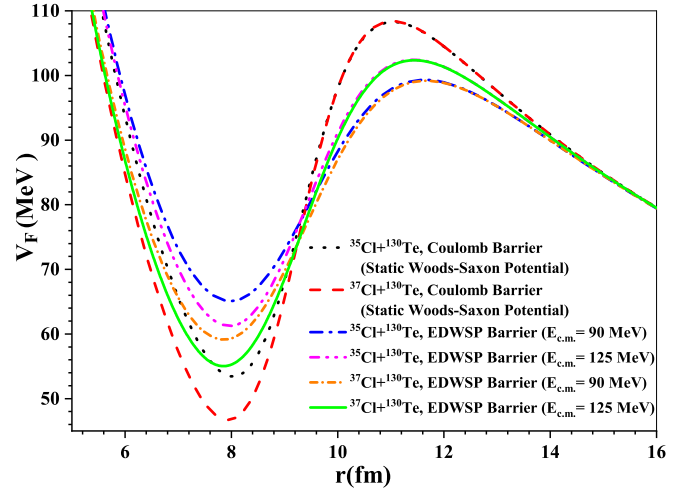


FIG. 5. Comparison of radial dependence of the fusion barriers for $^{35,37}\text{Cl} + ^{130}\text{Te}$ reactions produced by using the static Woods-Saxon potential and the EDWSP fusion barrier at different incident energies $E_{c.m.} = 90$ and 125 MeV. Similar behavior of the EDWSP barriers has been found at other incident energies ($E_{c.m.}$).

arising from nucleon-nucleon interactions. As the collision energy transitions from below to above the barrier region, the shallow nature of the EDWSP fusion barriers diminishes, leading to a reduction in the Pauli repulsion effect. This effect becomes saturated at energies significantly above the Coulomb barrier. This observation suggests that the EDWSP model inherently incorporates the impacts of nuclear matter incompressibility, nonlocal quantum effects, Pauli repulsion, and nucleon-nucleon interactions during the fusion process. This behavior is consistent for both $^{35,37}\text{Cl} + ^{130}\text{Te}$ reactions. Hence, the EDWSP model due to its energy-dependent nature effectively encompasses the relevant channel couplings stemming from nuclear structure, nucleon transfer channels, nuclear matter incompressibility, nonlocal quantum effects, and the Pauli repulsion effect during quantum mechanical tunneling along the fusion path, and appropriately reproduces the fusion dynamics of $^{35,37}\text{Cl} + ^{130}\text{Te}$ reactions in the domain of the Coulomb barrier.

B. Fragmentation analysis of compound systems $^{165,167}\text{Tm}^*$

Upon comprehending the detailed dynamics governing the entire fusion processes of $^{35,37}\text{Cl} + ^{130}\text{Te}$ reactions over the energy range $E_{c.m.} = 90 - 125$ MeV, it becomes imperative to explore the intricacies of the subsequent decay mechanisms exhibited by the resulting odd mass compound systems, namely $^{165,167}\text{Tm}^*$ [27,28]. In these selected reactions, the decay path involves the generation of evaporation residues (ERs), characterized by light fragment masses ($A_2 = 1 - 4$). To explore this decay channel, the dynamical cluster-decay model (DCM) [17–26] is employed. These calculations are conducted with a focus on the modulation of the neck formation (ΔR) during the binary fragmentation process, spanning the center-of mass-energy range ($E_{c.m.}$) of 90 to 125 MeV, specifically for quadrupole (β_2) deformed fragments characterized by hot configurations and optimized orientations.

TABLE III. The calculated cross sections for the ER decay channel originating from the isotopic systems $^{165,167}\text{Tm}^*$, which are produced through the $^{35}\text{Cl} + ^{130}\text{Te}$ and $^{37}\text{Cl} + ^{130}\text{Te}$ reactions, are systematically presented within the energy range of $E_{c.m.} = 93 - 121$ MeV. Alongside, a comprehensive inclusion of the crucial parameters integral to the dynamical cluster-decay model (DCM) are also presented, and the Coulomb barriers for the chosen systems are 105.14 and 104.2 MeV respectively for ^{35}Cl and ^{37}Cl reactions.

S. No.	$E_{c.m.}$	$^{35}\text{Cl} + ^{130}\text{Te} \rightarrow ^{165}\text{Tm}^*$					$^{37}\text{Cl} + ^{130}\text{Te} \rightarrow ^{167}\text{Tm}^*$				
		T (MeV)	ΔR (fm)	ℓ_{\max} (\hbar)	σ_{DCM} (mb)	$\sigma_{\text{expt.}}$ (mb)	T (MeV)	ΔR (fm)	ℓ_{\max} (\hbar)	σ_{DCM} (mb)	$\sigma_{\text{expt.}}$ (mb)
1	94.0	1.528	0.98	105	0.0327	0.034 ± 0.010	1.437	0.91	106	0.001	0.0012 ± 0.0005
2	95.6	1.556	1.08	122	0.221	0.243 ± 0.045	1.467	0.97	118	0.011	0.012 ± 0.0001
3	100.3	1.638	1.38	122	15.2	15.6 ± 1.8	1.566	1.36	120	14.65	14.70 ± 1.65
4	105.3	1.716	1.59	122	113.2	111 ± 13	1.645	1.57	121	112.9	115 ± 14
5	109.8	1.792	1.70	125	283.8	286 ± 23	1.734	1.68	125	311.7	313 ± 34
6	116.9	1.898	1.78	126	565.8	548 ± 70	1.806	1.75	126	472.2	473 ± 55
7	121.60	1.965	1.80	127	651.3	659 ± 83	1.876	1.80	127	646.3	648 ± 75

Table III offers a comparative insight into the DCM-calculated ER-decay cross sections originating from $^{165,167}\text{Tm}^*$ systems, compared with the corresponding experimental data across the energy range of interest. Upon scrutiny, a visible trend emerges: at lower energies, particularly within the sub-barrier region, the cross sections for the lighter system, $^{165}\text{Tm}^*$, exhibit enhanced values compared to the cross sections of the heavier counterpart, $^{167}\text{Tm}^*$. However, as the incident energy transitions to the above-barrier regime, the cross sections for the two systems become comparable. This observation is further corroborated by the behavior of the neck-length parameter required to accurately reproduce the experimental data. Specifically, in sub-barrier regions, the lighter system $^{165}\text{Tm}^*$ necessitates a higher neck-length parameter, while at energies surpassing the Coulomb barrier the neck length values tend to converge. The underlying cause for this enhancement in excitation functions, often referred to as ‘‘fusion enhancement,’’ is attributed to the dynamical interplay of factors encompassing the structural attributes, shell effects, and deformation configurations belonging to the decaying fragments. These facets will be further investigated in subsequent sections, shedding light on the nuanced interplay that contributes to the observed phenomena.

The cross sections obtained through the DCM exhibit a distinct dependence on the angular momentum (ℓ) values, encompassing the summation over the range $\ell = \ell_{\min}$ to $\ell = \ell_{\max}$. Also, the DCM based cross sections are a product of P_0 and P , which show contrasting behavior with increasing ℓ , hence the cumulative effect of ℓ is reflected in the DCM cross sections. On one hand, P_0 values for lighter fragments possesses higher magnitudes at $\ell \rightarrow 0\hbar$, and diminish at a certain maximum value, tagged as ℓ_{\max} ; on the other hand, P (for lighter fragments) shows noticeable magnitudes only above a certain minimum value termed as ℓ_{\min} . So, beyond this ℓ_{\min} to ℓ_{\max} window, the net contribution of preformation and penetration probabilities will be zero. This interplay between cross sections and angular momentum is exemplified in Fig. 6, where the decay cross sections for two specific decay channels, (a) $^{165}\text{Tm}^* \rightarrow ^{164}\text{Tm} + 1n$ and (b) $^{167}\text{Tm}^* \rightarrow ^{166}\text{Tm} + 1n$, are presented for the experimentally accessible energy spectrum. Interestingly, the ℓ window gets broader with increasing center-of-mass energy, for both the chosen

systems, which represents an increase in the $1n$ -decay cross sections with increase in $E_{c.m.}$. A noteworthy point here can be seen through the position of the ℓ window for both cases. ℓ_{\min} represents the position where penetration probability starts contributing significantly towards reaction cross sections, and the shift of ℓ_{\min} values towards lower magnitude as $E_{c.m.}$ increases indicates that penetration of the decaying fragments/nuclei requires lower centrifugal energy at higher $E_{c.m.}$ values. This also reflects the dependence of penetration probability on angular momentum states. On the other hand, the ℓ_{\max} value (which is decided by the diminishing of P_0) seems to be consistent at all the $E_{c.m.}$ values, signifying that the preformation probability possesses a weaker dependence on $E_{c.m.}$ values. So the dependence of channel cross sections on ℓ is decided by the dependence of P_0 and P , and the cumulative effect is reflected in Fig. 6; this observation is consistent for both the isotopic compound nuclear systems. In essence, the examination of DCM-based cross sections in relation to angular momentum values reveals the

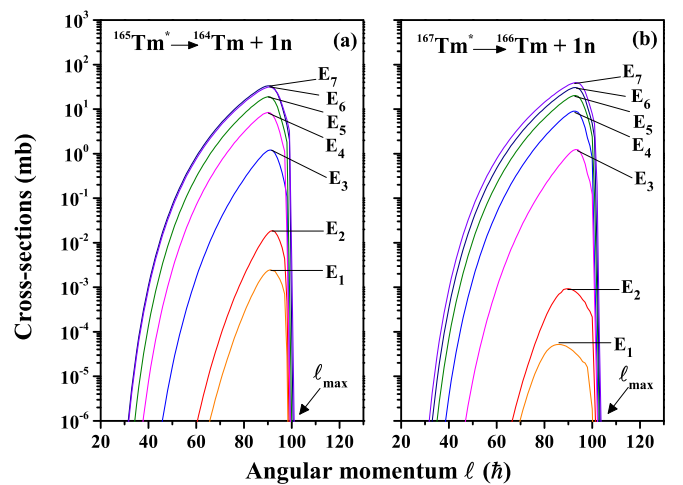


FIG. 6. Variation of DCM calculated channel cross sections plotted for (a) $^{165}\text{Tm}^* \rightarrow ^{164}\text{Tm} + 1n$ and (b) $^{167}\text{Tm}^* \rightarrow ^{166}\text{Tm} + 1n$ as a function of angular momentum state of the system. The data is presented across all the reported energies ranging from $E_{c.m.} = 93 - 121$ MeV mentioned in Table III indicated as E_1 to E_7 .

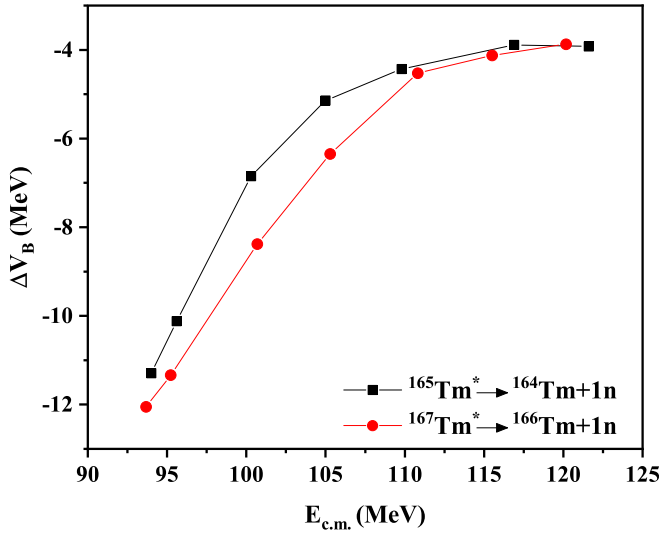


FIG. 7. The barrier lowering parameter ΔV_B plotted for $^{165}\text{Tm}^* \rightarrow ^{164}\text{Tm} + 1n$ and $^{167}\text{Tm}^* \rightarrow ^{166}\text{Tm} + 1n$ channel, over the center of mass energy range $E_{c.m.} = 93\text{--}121$ MeV.

complex dynamics that shed light on the quantum tunneling mechanisms governing the decay processes of the $^{165,167}\text{Tm}^*$ systems formed in the $^{35,37}\text{Cl} + ^{130}\text{Te}$ reactions.

In the study using the dynamical cluster-decay model (DCM), understanding the behavior of a crucial parameter, ΔV_B , is essential. This parameter plays a pivotal role in calculations related to the Coulomb barrier and to understand the behavior of potential barrier. To comprehend this, it is important to carefully analyze ΔV_B values in terms of the range of energies around the Coulomb barrier. ΔV_B is a metric that represents the difference between the effective barrier faced by a fragment undergoing decay (represented as V_{R_d}) and the actual height of the barrier (V_B). Notably, ΔV_B is always negative, indicating a decrease from the barrier height. Figure 7 visually depicts a noticeable trend: as the energy of the center of mass ($E_{c.m.}$) increases for the decay channel $^{164}\text{Tm} + 1n$, the magnitude of ΔV_B decreases. These values of ΔV_B correspond to a specific ℓ_{\min} value at a given $E_{c.m.}$. This decreasing trend in the magnitude of ΔV_B suggests that, as the energy of the system increases, there is a reduction in the potential barrier, hence a lesser barrier modification is required. A similar trend is observed for the heavier isotope $^{167}\text{Tm}^*$, with a slight change in magnitude. In simpler terms, the study indicates that, as the energy of the decaying system increases, there tends to be a decrease in the potential barrier, and this trend holds true for different isotopes, albeit with some variations.

In addition to this, the preformation probability (P_0) holds a paramount significance and provides valuable insights into the structural attributes of the decaying compound nucleus, explicitly relying on the mass numbers of the decaying fragments (A_1 and A_2) and the temperature (T) characterizing the hot-rotating compound nucleus. The influence of temperature is introduced via the center-of-mass energy of the incident channel ($E_{c.m.}$). To illustrate the intricacies of P_0 , Fig. 8 portrays the variation of ℓ -summed P_0 with A_2 and $E_{c.m.}$, with a focus on the decay process emanating from

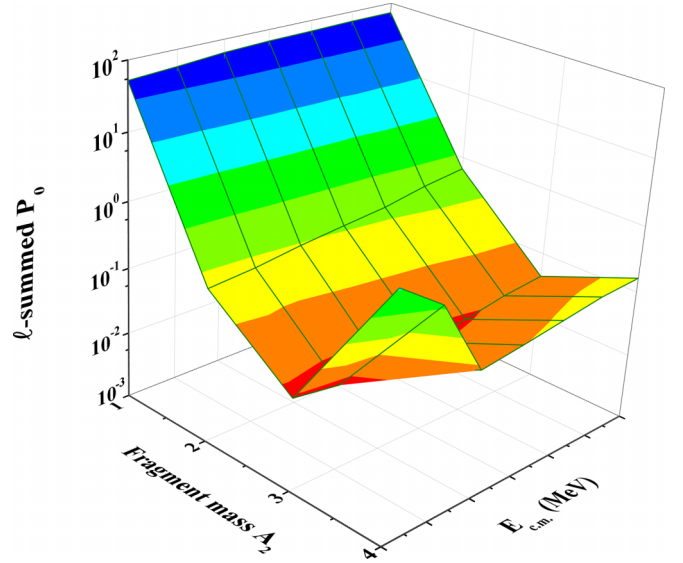
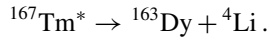
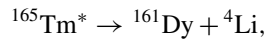


FIG. 8. ℓ -summed preformation probability (summed up to ℓ_{\max}) of decaying fragments with mass $A_2 = 1\text{--}4$, plotted over the entire energy range for the $^{165}\text{Tm}^*$ nucleus.

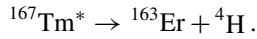
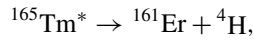
the $^{165}\text{Tm}^*$ nucleus. It is noteworthy that the depicted curve encompasses the realm of light particle masses, and spans all reported energies ($E_{c.m.} = 90$ to 125 MeV). This depiction of ℓ -summed P_0 entails the aggregation of P_0 values across all angular momentum states up to ℓ_{\max} . A detailed examination of the figure illuminates yields some salient observations:

- (i) Among the different decay channels, the $1n$ -emission channel exhibits notably higher preformation probabilities across all available energies, followed by ^2H - and ^3H -decay channels. This implies that the formation of the lanthanide nucleus ^{164}Tm is energetically favored in comparison to the isotopes ^{163}Er and ^{162}Er . Remarkably, this trend remains consistent across all the reported energy values.
- (ii) Further examination of the decay channel with $A_2 = 4$ reveals intriguing structural variations. Specifically, it indicates that the fragment associated with $A_2 = 4$ exhibits higher P_0 values at lower energies, compared to higher energies, where the curve displays a smoother progression. This peculiar behavior can be attributed to the identity of the fragment at these energy levels. At lower energies, the fragment with $A_2 = 4$ corresponds to ^4Li , which is unstable and subsequently decays into ^3He via p emission, and then into deuterium (d) via $2p$ emission. Conversely, at higher energies, the synthesis of ^{161}Er is facilitated through ^4H emission. Once again, ^4H 's instability leads to its decay via n emission into tritium (t), which subsequently decays into deuterium (d). This intriguing observation underscores the notion that different light particles are preformed at distinct $E_{c.m.}$ values. Also, the preferential minimization of a specific fragment associated with a light fragment mass number $A_2 = 4$ holds the potential to shed light on the observed

fusion enhancement in the lighter system $^{165}\text{Tm}^*$. As expounded earlier, particularly at below-barrier energies, distinct decay channels manifest themselves as follows:



Conversely, at above-barrier energies, the decay channels unfold as



In the context of sub-barrier energies, a noteworthy distinction emerges with regard to the deformation parameters governing the daughter nuclei that emerge subsequent to the evaporation of ^4Li , characterized by a deformation parameter of $\beta_2 = -0.328$. Specifically, for the daughter nuclei ^{161}Dy and ^{163}Dy , the resulting deformation parameters are observed to be $\beta_2 = 0.307$ and $\beta_2 = 0.327$ respectively. It becomes evident that the prolate deformations exhibited by the daughter nucleus emerging from the heavier isotope are notably more pronounced than those manifested by the lighter isotopic compound nucleus. Within the framework of the dynamical cluster-decay model (DCM), the role of deformations assumes a significant role. DCM specifically engages with the dynamics of decay processes, and, as such, the deformations inherent to the fragments undergoing decay, as well as the exit channel partners, play a pivotal role. Consequently, the augmented prolate deformations found in ^{163}Dy are postulated to exert a considerable influence on the fusion process. In summation, this insight may provide a comprehensive perspective on the observed disparities in excitation functions between the $^{167}\text{Tm}^*$ and $^{165}\text{Tm}^*$ systems, particularly in the context of sub-barrier energies.

In the broader context, it is crucial to highlight that a fragment's net contribution to the total decay cross sections is determined by the product of preformation probability and penetration probability, denoted as P_0P . Therefore, it becomes imperative to interrogate the variation of the penetration probability in terms of the light fragment mass A_2 and the center-of-mass energy $E_{c.m.}$. This comprehensive analysis is important for understanding the quantum tunneling process, structural attributes, and energy dependencies that govern the intricate dynamics of decay in the $^{165,167}\text{Tm}^*$ systems formed through the $^{35,37}\text{Cl} + ^{130}\text{Te}$ reactions. This phenomenon is further illuminated through Fig. 9, which provides an insightful portrayal of the ℓ -summed penetration probability (P) in the context of decaying fragments with varying mass numbers $A_2 = 1-4$, originating from the complex nucleus $^{165}\text{Tm}^*$. The curve exhibited in this figure unveils a compelling contrast, one that reveals intriguing insights into the behavior of the barrier penetration probabilities. Within this context, the barrier penetration probabilities associated with the $A_2 = 1$ fragment, signifying the $1n$ -emission channel, stand out for their relatively subdued magnitudes when compared against the counterparts representing fragments with $A_2 = 2$ and 3 , corresponding to the ^2H - and ^3H -emission channels

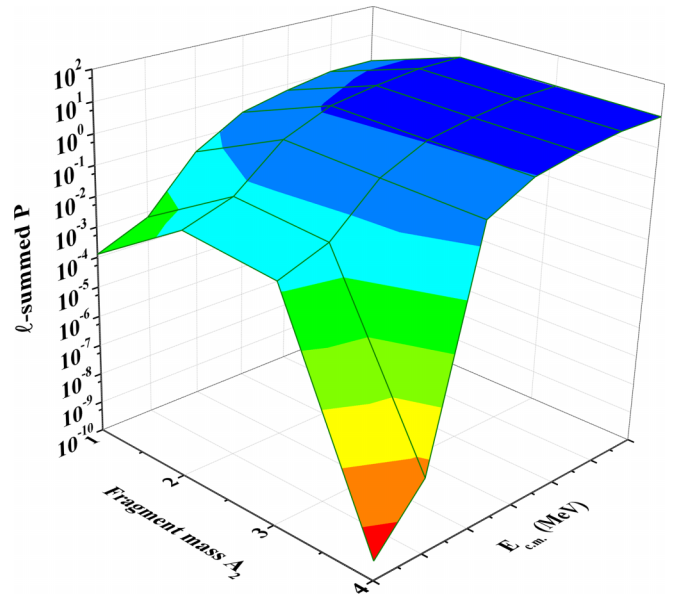


FIG. 9. ℓ -summed tunneling probability (summed up to ℓ_{\max}) of decaying fragments with mass $A_2 = 1-4$, plotted over the entire energy range for the $^{165}\text{Tm}^*$ nucleus.

respectively. This observation consistently holds true across the entirety of the spectrum of available center-of-mass energies ($E_{c.m.}$). Remarkably, a distinctive behavior emerges for the light fragment characterized by a mass number $A_2 = 4$. This behavior is particularly evident as $E_{c.m.}$ transitions from the below-barrier region to the above-barrier region. At the lower energies, the barrier penetration probability values exhibit an extremely subdued nature, seemingly indicating a diminished likelihood of penetration. In contrast, as $E_{c.m.}$ escalates to higher levels, the barrier penetration probabilities for this fragment become comparable to those witnessed in the case of the ^2H - and ^3H -emission channels. Strikingly, the barrier penetration probabilities for $A_2 = 4$ become notably higher than those associated with the $1n$ channel. To discern the origins of these contrasting behaviors, it is instructive to revisit the earlier discussion. The exceptionally low barrier penetration probabilities observed at lower energies may be attributed to the emission of distinct fragments, particularly in the context of ^4Li emission. This specific emission mode, accompanied by $^3\text{He}-p$ or $d2p$ emissions, appears to be characterized by an inherently low penetration probability. On the other hand, the heightened barrier penetration probabilities associated with $A_2 = 4$ at higher energies, akin to ^2H and ^3H emissions, seem to align with the emission of ^4H fragments (or equivalently, tn or $d2n$ emissions). This intricate interplay between mass numbers, fragment emissions, and barrier penetration probabilities provides a nuanced understanding of the fusion dynamics and sheds light on the mechanisms underlying the observed variations in penetration probabilities across different energy regimes.

Importantly, the DCM-calculated cross sections reside in the meshing between two pivotal factors, namely P_0 and P . The synergy between these quantities is brought into focus by the cross sections derived from DCM for fragments with

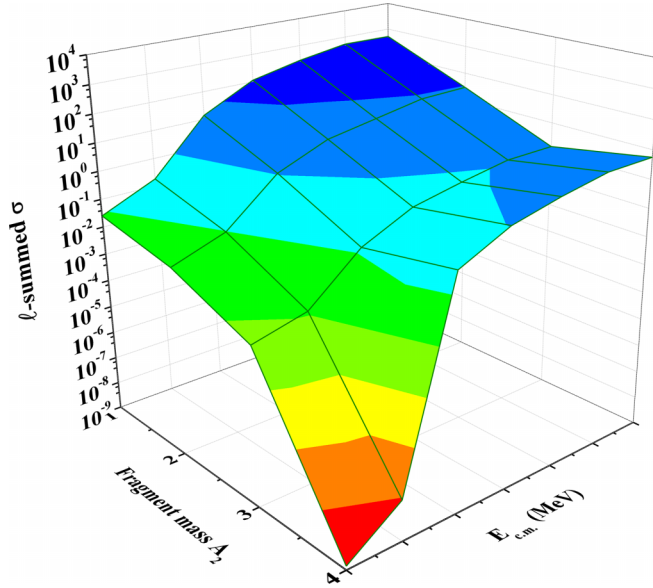


FIG. 10. ℓ -summed DCM cross sections (summed up to ℓ_{\max}) of decaying fragments with mass $A_2 = 1-4$, plotted over the entire energy range for the $^{165}\text{Tm}^*$ nucleus.

varying mass numbers $A_2 = 1-4$, emitted from the nucleus $^{165}\text{Tm}^*$. This symbiotic relationship unfolds in the context of center-of-mass energy ($E_{c.m.}$) and is portrayed in Fig. 10. This figure combines information from Figs. 8 and 9 to help us see how these factors are connected. Upon closer examination, it becomes apparent that the $1n$ -emission channel exerts the most substantial influence on the cumulative DCM cross sections for the ER-decay channel stemming from $^{165}\text{Tm}^*$. It is noteworthy that, although the P values attributed to the $1n$ -emission are relatively modest, their amplification by higher P_0 values serves to magnify the overall $1n$ cross sections. Interestingly, a slightly different scenario unfolds for fragments characterized by $A_2 = 4$. In this context, the P_0 values outshine those associated with fragments $A_2 = 2$ and 3 (^2H and ^3H), but the substantially subdued P values, especially at lower energies, curtail their contribution to the aggregate ER cross sections to negligible levels. This insight yields a crucial finding: the channel cross sections pertaining to the ^4Li fragment ($^3\text{He}-p$ or $d2p$) are inherently negligible, as is strikingly evident in the below-barrier energy region. However, a remarkable transformation occurs for $A_2 = 4$ as $E_{c.m.}$ ascends to higher values, heralding a transition to the ^4H decay channel (tn or $d2n$). This transition brings with it a substantial elevation in DCM cross sections, emphasizing the channel's promising significance. In summation, the complexities underlying the DCM-calculated cross sections come into sharp focus. At lower energies, the dominant channel is $1n$; the contribution of this channel is propelled by the synergistic interplay between enhanced P_0 values and comparatively modest P values. However, as the energy trajectory ascends, the collective contributions of other decay channels, including ^2H , ^3H , and ^4H ($^3\text{He}-n$ or $d2n$), assert themselves with marked significance. This unique interplay between the various decay channels and the values of P_0 and P provides a

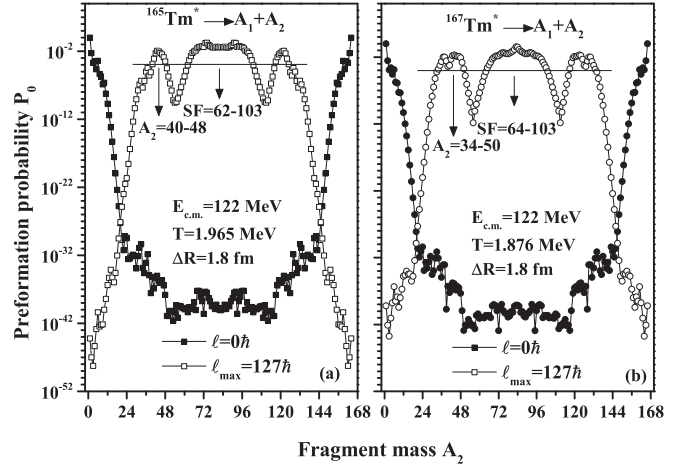


FIG. 11. Structural variation of preformation probability P_0 for (a) $^{165}\text{Tm}^*$ and (b) $^{167}\text{Tm}^*$ in terms of fragment mass A_i at $E_{c.m.} = 122$ MeV and best fit values of neck-length parameter. The graph is plotted at $\ell = 0\hbar$ and ℓ_{\max} values.

comprehensive understanding of the fusion dynamics and the modulation of cross sections as a function of energy.

Finally, a thorough structural analysis has been conducted in Fig. 11 for the decaying nuclei $^{165}\text{Tm}^*$ and $^{167}\text{Tm}^*$. In this context, the preformation probability, denoted as P_0 , has been meticulously plotted against the fragment mass number A_i at the highest energy $E_{c.m.} = 122$ MeV, employing the respective best-fit values of the neck-length parameter. The resulting curve has been generated for extreme momentum values, revealing intriguing insights. Notably, at lower angular momentum states, the preformation probability values exhibit a preference for the lighter mass region, indicating it to be the favored decay mode for both chosen systems. However, as higher angular momentum states are considered, a discernible change in the structural dynamics becomes evident. For both systems, an elevation in the magnitude of preformation probability is observed, particularly in the heavy mass and fission regions. The graphical representation identifies highly preformed peaks in the symmetric fission region and the asymmetric heavy mass region. It is noteworthy that the net contribution of these mass fragments to the total decay cross sections is contingent upon their penetration probability values. The emergence of asymmetric peaks in the heavy mass region is attributed to the shell closure at $Z_2 = 20$, while a corresponding occurrence in the symmetric fission region is due to the magic shell closure at $Z_1 = 50$. Remarkably, the placement of these peaks is nearly identical in both isotopic systems, although the addition of two neutrons in the heavier system does influence the mass spectrum of these peaks to some extent. Upon comparing the odd mass structure of $^{165}\text{Tm}^*$ or $^{167}\text{Tm}^*$ with the even mass systems $^{98,104}\text{Cd}^*$ formed in $^{40}\text{Ca} + ^{58,64}\text{Ni}$ reactions, it becomes evident that, for the odd mass systems, the decay profile is broadly symmetric, with a significant contribution from asymmetric shoulders in the heavy mass region. Conversely, in the case of even mass systems, the structure/decay profile is predominantly symmetric, with contributing asymmetric shoulders lying in

the intermediate mass region. Furthermore, a comparative analysis of the decay profile of even mass systems $^{122,128}\text{Ba}^*$ lends support to the notion of asymmetric shoulders in the intermediate mass region. Notably, no such contribution from intermediate mass fragments is observed for the selected odd systems. This comprehensive analysis provides a nuanced understanding of the structural intricacies and decay characteristics of the studied nuclei.

IV. SUMMARY AND CONCLUSIONS

The investigation of $^{35,37}\text{Cl} + ^{130}\text{Te}$ reactions employs the energy-dependent Woods-Saxon potential (EDWSP) model to comprehensively analyze fusion dynamics. At the lowest incident energy ($E_{\text{c.m.}} = 90$ MeV) with a large diffuseness parameter ($a = 0.982$ fm), the calculated lowest energy-dependent fusion barrier (LEDFB) is significantly lower than the Coulomb barriers, indicating a prominent barrier-lowering effect of the EDWSP model. This effect is most pronounced at the lowest incident energy, suggesting maximum modulations during the fusion process. As the incident energy increases and the diffuseness parameter decreases, the EDWSP's impact on the fusion barrier diminishes, resulting in a reduction in the interaction barrier height. Notably, the experimental cross sections for $^{35,37}\text{Cl} + ^{130}\text{Te}$ reactions align well with the EDWSP model, and no fusion hindrance is observed in either system. The sub-barrier fusion enhancement in $^{35}\text{Cl} + ^{130}\text{Te}$ compared to $^{37}\text{Cl} + ^{130}\text{Te}$ is attributed to the combined effects of odd- A spin states of the projectile and the positive Q -value neutron transfer channel, particularly the dominant pair neutron transfer channel. Coupled channel analysis and EDWSP calculations reveal similar conclusions, highlighting the influences of positive Q -value neutron transfer channels and inelastic surface excitations of the collision partners. The EDWSP model, by incorporating the energy-dependent

nature of diffuseness, effectively lowers the fusion barrier, enhancing the predictive power of the model and providing a reasonable explanation for the fusion dynamics in $^{35,37}\text{Cl} + ^{130}\text{Te}$ reactions.

Further, the study explores into the detailed dynamics of $^{35,37}\text{Cl} + ^{130}\text{Te}$ reactions within the energy range $E_{\text{c.m.}} = 90$ – 125 MeV, focusing on the subsequent decay mechanisms of the resulting odd mass compound systems, $^{165,167}\text{Tm}^*$. Utilizing the dynamical cluster-decay model (DCM), the analysis explores the modulation of neck formation during binary fragmentation processes, emphasizing quadrupole-deformed fragments. Comparative insights into DCM-calculated ER-decay cross sections for $^{165,167}\text{Tm}^*$ systems reveal intriguing trends, such as fusion enhancement at sub-barrier energies and convergence at above-barrier regimes. The dependence of cross sections on angular momentum values and the behavior of the crucial parameter ΔV_B around the Coulomb barrier are elucidated. The preformation probability (P_0) and its interplay with penetration probability (P) are highlighted, unraveling the complex dynamics governing the decay processes. Structural analysis of $^{165,167}\text{Tm}^*$ nuclei showcases preferential decay modes, peak formations, and the influence of shell closures. A comparison with even mass systems provides further insights into the symmetry and asymmetry of decay profiles. The study concludes with a comprehensive understanding of the structural intricacies and decay characteristics of the studied nuclei, shedding light on the quantum tunneling mechanisms governing their decay processes.

ACKNOWLEDGMENT

One of us (G.S.) is thankful to the Department of Science and Technology, Government of India for financial support through “DST/WOS-A/PM-53/2021” under Women Scientists Scheme A. M.K.S. is thankful to DST-SERB for Grant No. CRG/2021/001144.

-
- [1] M. Beckerman, *Rep. Prog. Phys.* **51**, 1047 (1988).
 [2] M. Dasgupta *et al.*, *Annu. Rev. Nucl. Part. Sci.* **48**, 401 (1998).
 [3] A. B. Balantekin and N. Takigawa, *Rev. Mod. Phys.* **70**, 77 (1998).
 [4] L. P. Canto *et al.*, *Phys. Rep.* **424**, 1 (2006).
 [5] B. B. Back, H. Esbensen, C. L. Jiang, and K. E. Rehm, *Rev. Mod. Phys.* **86**, 317 (2014).
 [6] Ş. Mişicu, *Int. J. Mod. Phys. E* **23**, 1450074 (2014).
 [7] S. J. Sanders, D. G. Kovar, B. B. Back, C. Beck, D. J. Henderson, R. V. F. Janssens, T. F. Wang, and B. D. Wilkins, *Phys. Rev. C* **40**, 2091 (1989).
 [8] S. J. Sanders, *Phys. Rev. C* **44**, 2676 (1991).
 [9] T. Matsuse, C. Beck, R. Nouicer, and D. Mahboub, *Phys. Rev. C* **55**, 1380 (1997).
 [10] R. Vandenbosch and J. R. Huizenga, *Nuclear Fission* (Academic Press, New York, 1973).
 [11] L. G. Moretto, *Nucl. Phys. A* **247**, 211 (1975).
 [12] M. S. Gautam, A. Kaur, and M. K. Sharma, *Phys. Rev. C* **92**, 054605 (2015).
 [13] J. Kaur, A. Kaur, M. S. Gautam, and M. K. Sharma, *Phys. Rev. C* **106**, 034615 (2022).
 [14] M. Singh *et al.*, *Mod. Phys. Lett. A* **26**, 2129 (2011).
 [15] M. Singh *et al.*, *Nucl. Phys. A* **897**, 179 (2013).
 [16] M. S. Gautam, *Phys. Rev. C* **90**, 024620 (2014).
 [17] R. K. Gupta, in *Clusters in Nuclei*, edited by C. Beck, Lecture Notes in Physics Vol. 818 (Springer, Berlin, 2010), Vol. 1, pp. 223–264.
 [18] R. K. Gupta, M. Balasubramaniam, R. Kumar, D. Singh, and C. Beck, *Nucl. Phys. A* **738**, 479 (2004); M. Kaur and M. K. Sharma, *Eur. Phys. J. A* **50**, 61 (2014).
 [19] R. K. Gupta, S. K. Arun, R. Kumar, and M. Bansal, *Nucl. Phys. A* **834**, 176c (2010).
 [20] D. Jain, R. Kumar, M. K. Sharma, and R. K. Gupta, *Phys. Rev. C* **85**, 024615 (2012).
 [21] R. Kumar, K. Sandhu, M. K. Sharma, and R. K. Gupta, *Phys. Rev. C* **87**, 054610 (2013); K. Sandhu, G. Kaur, and M. K. Sharma, *Nucl. Phys. A* **921**, 114 (2014).
 [22] G. Sawhney and M. K. Sharma, *Eur. Phys. J. A* **48**, 57 (2012); G. Kaur and M. K. Sharma, *Phys. Rev. C* **87**, 044601 (2013);

- G. Kaur, D. Jain, R. Kumar, and M. K. Sharma, *Nucl. Phys. A* **916**, 260 (2013).
- [23] A. Kaur and M. K. Sharma, *Mod. Phys. Lett. A* **35**(11), 2050082 (2020).
- [24] A. Kaur and M. K. Sharma, *Nucl. Phys. A* **957**, 274 (2017).
- [25] A. Kaur, K. Sandhu, G. Sawhney, and M. K. Sharma, *Eur. Phys. J. A* **58**, 59 (2022).
- [26] G. Sawhney, A. Kaur, M. K. Sharma, and R. K. Gupta, *Phys. Rev. C* **92**, 064303 (2015).
- [27] R. N. Sahoo, M. Kaushik, A. Sood *et al.*, *Phys. Rev. C* **102**, 024615 (2020).
- [28] R. N. Sahoo, M. Kaushik, A. Sood *et al.*, *Phys. Rev. C* **99**, 024607 (2019).
- [29] G. Montagnoli and A. M. Stefanini, *Eur. Phys. J. A* **53**, 169 (2017).
- [30] C. L. Jiang *et al.*, *Eur. Phys. J. A* **57**, 235 (2021).
- [31] K. Hagino and N. Takigawa, *Prog. Theor. Phys.* **128**, 1061 (2012).
- [32] C. H. Dasso, S. Landowne, and A. Winther, *Nucl. Phys. A* **405**, 381 (1983).
- [33] C. H. Dasso, S. Landowne, and A. Winther, *Nucl. Phys. A* **407**, 221 (1983).
- [34] C. H. Dasso and S. Landowne, *Comput. Phys. Commun.* **46**, 187 (1987).
- [35] J. Fernández-Niello, C. H. Dasso, and S. Landowne, *Comput. Phys. Commun.* **54**, 409 (1989).
- [36] K. Hagino, N. Rowley, and A. T. Kruppa, *Comput. Phys. Commun.* **123**, 143 (1999).
- [37] C. Simenel, A. Wakhle, and B. Avez, *J. Phys.: Conf. Ser.* **420**, 012118 (2013).
- [38] A. S. Umar, C. Simenel, and V. E. Oberacker, *Phys. Rev. C* **89**, 034611 (2014).
- [39] A. S. Umar and V. E. Oberacker, *Eur. Phys. J. A* **39**, 243 (2009).
- [40] Vijay, R. P. Chahal, M. S. Gautam, S. Duhan, and H. Khatri, *Phys. Rev. C* **103**, 024607 (2021).
- [41] Vijay, R. P. Chahal, S. Duhan, H. Khatri, and M. S. Gautam, *Int. J. Mod. Phys. E* **30**, 2150075 (2021).
- [42] Vijay, N. Grover, K. Sharama, M. S. Gautam, M. K. Sharma, and R. P. Chahal, *Phys. Rev. C* **106**, 064609 (2022).
- [43] Vijay, M. S. Gautam, R. P. Chahal, S. Duhan, and H. Khatri, *Phys. Scr.* **97**, 045305 (2022).
- [44] V. Ghanghas, R. P. Chahal, S. Duhan, H. Khatri, and M. S. Gautam, *Braz. J. Phys.* **52**, 84 (2022).
- [45] V. N. Kondratyev, A. Bonasera, and A. Iwamoto, *Phys. Rev. C* **61**, 044613 (2000).
- [46] D. Vautherin and D. M. Brink, *Phys. Rev. C* **5**, 626 (1972).
- [47] S. Krewald, V. Klemm, J. Speth, and A. Faessler, *Nucl. Phys. A* **281**, 166 (1977).
- [48] H. S. Köhler, *Nucl. Phys. A* **258**, 301 (1976).
- [49] B. K. Agrawal, S. K. Dhiman and R. Kumar, *Phys. Rev. C* **73**, 034319 (2006).
- [50] M. Dutra, O. Lourenco, J. S. SaMartins, A. Delfino, J. R. Stone, and P. D. Stevenson, *Phys. Rev. C* **85**, 035201 (2012).
- [51] D. L. Hill and J. A. Wheeler, *Phys. Rev.* **89**, 1102 (1953).
- [52] C. Y. Wong, *Phys. Rev. Lett.* **31**, 766 (1973).
- [53] J. O. Newton, R. D. Butt, M. Dasgupta, D. J. Hinde, I. I. Gontchar, C. R. Morton, and K. Hagino, *Phys. Rev. C* **70**, 024605 (2004).
- [54] A. Mukherjee, D. J. Hinde, M. Dasgupta, K. Hagino, J. O. Newton, and R. D. Butt, *Phys. Rev. C* **75**, 044608 (2007).
- [55] L. C. Chamon *et al.*, *Phys. Rev. C* **66**, 014610 (2002).
- [56] C. Simenel, M. Dasgupta, D. J. Hinde, and E. Williams, *Phys. Rev. C* **88**, 064604 (2013).
- [57] S. S. Malik and R. K. Gupta, *Phys. Rev. C* **39**, 1992 (1989).
- [58] S. K. Arun, R. K. Gupta, B. B. Singh, S. Kanwar, and M. K. Sharma, *Phys. Rev. C* **79**, 064616 (2009).
- [59] S. K. Arun, R. K. Gupta, S. Kanwar, B. B. Singh, and M. K. Sharma, *Phys. Rev. C* **80**, 034317 (2009).
- [60] J. Maruhn and W. Greiner, *Phys. Rev. Lett.* **32**, 548 (1974).
- [61] R. K. Gupta, W. Scheid, and W. Greiner, *Phys. Rev. Lett.* **35**, 353 (1975).
- [62] A. Săndulescu, R. K. Gupta, W. Scheid, and W. Greiner, *Phys. Lett. B* **60**, 225 (1976).
- [63] H. Kröger and W. Scheid, *J. Phys. G: Nucl. Phys.* **6**, L85 (1980).
- [64] P. A. Seeger, *Nucl. Phys.* **25**, 1 (1961).
- [65] N. J. Davidson, S. S. Hsiao, J. Markram, H. G. Miller, and Y. Tzeng, *Nucl. Phys. A* **570**, 61 (1994).
- [66] W. Myers and W. J. Swiatecki, *Nucl. Phys.* **81**, 1 (1966).
- [67] C. Simenel, A. S. Umar, K. Godbey, M. Dasgupta, and D. J. Hinde, *Phys. Rev. C* **95**, 031601(R) (2017).
- [68] W. Henning, Y. Eisen, H.-J. Körner, D. G. Kovar, J. P. Schiffer, S. Vigdor, and B. Zeidman, *Phys. Rev. C* **17**, 2245 (1978).
- [69] V. V. Sargsyan, G. G. Adamian, N. V. Antonenko, W. Scheid, and H. Q. Zhang, *Phys. Rev. C* **85**, 024616 (2012).
- [70] V. V. Sargsyan, G. G. Adamian, N. V. Antonenko, W. Scheid, and H. Q. Zhang, *Eur. Phys. J. A* **49**, 54 (2013).